



Cite this: *Chem. Commun.*, 2021, 57, 4420

Received 15th February 2021,  
Accepted 23rd March 2021

DOI: 10.1039/d1cc00868d

rsc.li/chemcomm

# Double intramolecular hydrogen transfer assisted dual emission in a carbazole-embedded porphyrin-like macrocycle†

Arumugan Kalaiselvan, Aswini Spergen, Isukapalli Sai Vamsi Krishna, ,  
Vennapusa Sivaranjana Reddy and Sabapathi Gokulnath \*

The introduction of a pyrrole ring at one of the *meso* positions of carbazole-based porphyrins lowers the structural symmetry and results in dual emission, which strongly depends on the excitation wavelength and temperature. The origin of dual emission induced by NH-tautomerism is confirmed *via* photophysical and DFT calculations.

NH tautomerism plays a vital role in developing molecular switches<sup>1,2</sup> and information storage.<sup>3</sup> In porphyrinoids, NH-tautomerism can be distinguishable and exhibit two different optical properties when porphyrin possesses irregular substitution leading to unsymmetrical structures on the cores (Fig. 1a).<sup>4</sup> Such NH tautomerism in porphyrins occurs stepwise through a *cis*-intermediate supported by tunnelling mechanism in solution (Fig. 1a).<sup>5,6</sup> The unequal ground and excited state energies in metal-free porphyrins result in a dual emission involving NH-tautomerism. Dual emitters (DEs) have gained immense attention recently due to their potential applications in various fields, such as sensors,<sup>7</sup> multicolour displays,<sup>8</sup> white organic light emitting diodes (WOLEDs),<sup>9</sup> data encryption<sup>10</sup> and bio-imaging.<sup>11,12</sup> Due to the close relation between NH-tautomerism and dual emission in various macrocyclic compounds, we devised a *meso*-modification strategy on the carbazole embedded porphyrin with a *meso*-pyrrole substituent. Such substitution provides nonsymmetric structures that can lead to two distinguishable pathways for the tautomeric process. Herein, efforts have been made to study whether the tautomerism can take place either *via* a step-wise or a simultaneous double intramolecular hydrogen transfer (DIHT). Specifically, NH-tautomerism in porphycenes (*trans* ⇌ *trans*) takes place simultaneously *via* concerted tunnelling from a

vibrationally excited level without populating its relatively high energy *cis*-intermediate.<sup>13,14</sup> In addition, porphycenes featuring an NH...N distance of 2.53 Å, which is relatively small as compared to porphyrin, and thereby exhibit dual-fluorescence. Interestingly, dual emission was also observed in corroles due to the coexistence of both tautomers (T1 and T2) even at a lower temperature (77 K), which suggests that the energy difference between these tautomers is very small (2.45 kcal mol<sup>-1</sup>).<sup>15,16</sup> Very recently, a *meso*-modified heteroporphyrin with the replacement of one methine carbon with

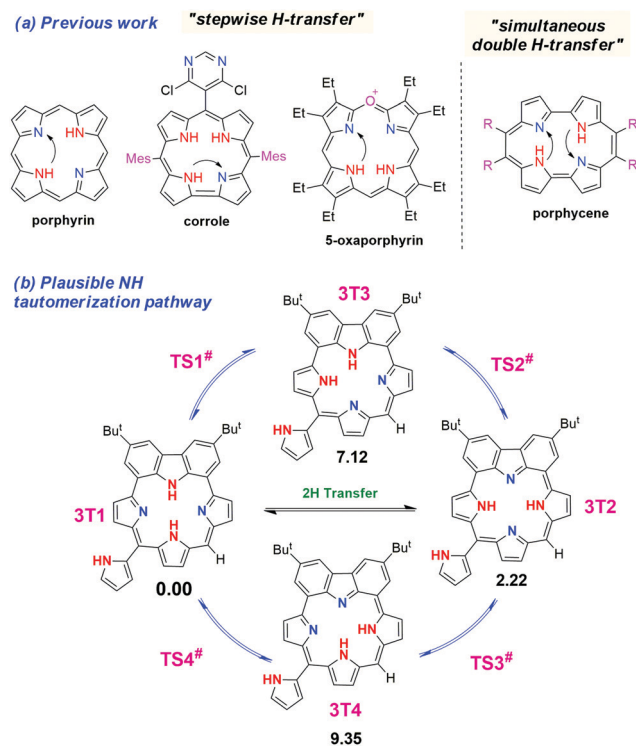


Fig. 1 (a) Selected examples of dual emitters. (b) A plausible pathway for NH-tautomerization between 3T1 and 3T2; the relative energy for each tautomer is given with the respective chemical structure (units: kcal mol<sup>-1</sup>).

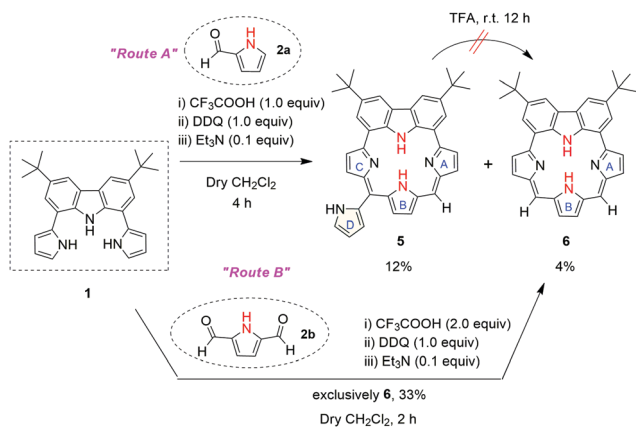
School of Chemistry, Indian Institute of Science Education and Research, Thiruvananthapuram-695551, Maruthamala P.O., Vithura, Kerala, India. E-mail: gokul@iisertvm.ac.in

† Electronic supplementary information (ESI) available: Experimental details and compound data. CCDC 2062803, 2059574 and 2059575. For ESI and crystallographic data in CIF or other electronic format see DOI: 10.1039/d1cc00868d

oxygen exhibited dual fluorescence through its unique NH-tautomerism.<sup>17</sup>

The syntheses of carbazole incorporated *meso*-pyrrole **3**, *meso*-unsubstituted **4** and *meso*-pentafluorophenyl substituted **5** porphyrin-like macrocycles are shown in Scheme 1. At first, we performed a “3+1” acid catalysed condensation reaction of **1**<sup>18</sup> with 1*H*-pyrrole-2-carbaldehyde **2a** in the presence of CF<sub>3</sub>COOH followed by DDQ oxidation to provide macrocycles **3** in 12% and **4** in 4%. The HRMS of **3** showed a distinct peak at  $m/z = 562.2961$  ( $[M + H]^+$ , calcd for C<sub>38</sub>H<sub>36</sub>N<sub>5</sub>:562.2971) (Fig. S3.5, ESI<sup>†</sup>) and **4** showed a molecular peak at  $m/z = 497.2709$  ( $[M + H]^+$ , calcd for C<sub>34</sub>H<sub>33</sub>N<sub>4</sub>:497.2705) (Fig. S3.6, ESI<sup>†</sup>). Considering the mass difference of one pyrrole moiety between **3** and **4**, diluted CF<sub>3</sub>COOH added to **3** did not produce **4**, thereby indicating that **4** was not derived from **3** during the reaction. All our attempts to improve the yield of **4** were unsuccessful, and hence we condensed **1** with 1*H*-pyrrole-2,5-dicarbaldehyde **2b** under similar conditions, which provided **4** in a surprisingly high yield of 33%. The <sup>1</sup>H NMR spectrum of **3** in CDCl<sub>3</sub> showed (Fig. S4.7, ESI<sup>†</sup>) a C<sub>s</sub> symmetric pattern with relatively upfield shifted signals for ring D correlating with each other in <sup>1</sup>H-<sup>1</sup>H COSY spectral analysis (Fig. S4.8, ESI<sup>†</sup>). Three singlets between 8.63 and 8.79 ppm are assigned to pyrrole and carbazole NHs, as confirmed by D<sub>2</sub>O experiments (Fig. S4.9, ESI<sup>†</sup>). Two closely associated multiplets at 7.27 and 7.31 ppm for ring B and three well separated multiplets between 7.64 and 8.08 ppm integrating to four protons are due to the two pyrrole rings (ring A and C).

In order to compare the optical and redox properties of **3** and **4**, a *bis-meso*-pentafluorophenyl substituted analogue **5** was also prepared by condensation of equimolar amounts of **1** with (perfluorophenyl)(1*H*-pyrrol-2-yl)methanol **6a**<sup>19</sup> in the presence of a catalytic amount of *para*-toluenesulfonic acid (*p*-TsOH) under an inert atmosphere for 2 h, followed by oxidation with 1.0 equiv. of DDQ (Route C and D, ESI<sup>†</sup>) in 19% yield. The initial characterization of **5** was performed using HRMS analysis which shows a molecular ion peak at  $m/z = 829.2374$  ( $[M + H]^+$ , calcd for C<sub>46</sub>H<sub>31</sub>F<sub>10</sub>N<sub>4</sub>:829.2374) and thus proved the exact composition of **5** (Fig. S3.7, ESI<sup>†</sup>). Alternatively, condensation of **7a**<sup>20</sup> with **1** also provided the macrocycle **5**,



**Scheme 1** Synthetic routes to the preparation of *meso*-pyrrolyl substituted carbazole embedded porphyrin **3**.

but in a slightly lower yield of 14% (route D in ESI<sup>†</sup>). The <sup>1</sup>H NMR spectra of **4** and **5** in CDCl<sub>3</sub> showed a simple spectral pattern attributed to their C<sub>2</sub> symmetric structures. The β-CHs of the pyrrole (ring B) in **4** and **5** resonate as singlets at 7.45 and 6.95 ppm, respectively. The two pyrrole rings (ring A) connected at the 1,8-positions of the carbazole subunit displayed two well-resolved doublets (7.64 ppm and 7.97 ppm for **4**; 7.48 ppm and 8.26 ppm for **5**) that are similar to what is seen in the case of **3** (Fig. S4.11 and S4.13, ESI<sup>†</sup>). The downfield shifts of the pyrrole and carbazole NH resonances in **4** and **5** are consistent with the existence of strong hydrogen-bonding interactions within the less shielded environment of N<sub>4</sub> cores.

Further insights into the molecular structure of **3** came from single crystal X-ray structural analyses of crystals obtained by the slow diffusion of methanol into a toluene solution of **3** at room temperature which crystallized in a triclinic crystal lattice with a P $\bar{1}$  space group (Table S6.1, ESI<sup>†</sup>). The structure is a nearly planar macrocycle with a tilted *meso*-pyrrole ring (ring D) by 53.9° and two adjacent pyrrole rings (rings B and C) were slightly inclined with respect to the mean plane (C5–C15–C25–C30) (Fig. 2a and b). Four intramolecular N–H···N hydrogen bonding interactions were observed inside the macrocycle (N1–H···N2:2.306 Å; N2–H···N3:2.360 Å; N3–H···N4:2.554 Å and N4–H···N1:2.458 Å), typical for regular porphyrins. Additionally, two strong intermolecular N–H···N hydrogen bonding interactions were also found with distances of 2.290 Å and 2.306 Å to form the self-assembled dimer (Fig. 2c). Similarly, the slow diffusion of methanol into a chloroform solution of **4** and **5** provided X-ray quality crystals of **4** and **5**. Both crystallized in a monoclinic crystal lattice with P2<sub>1</sub>/n and P2<sub>1</sub>/c space groups, respectively. The structures of both **4** and **5** revealed a more planar conformation and showed intramolecular N–H···N hydrogen bonding interactions typical for regular porphyrins (Fig. 3a and b).

The absorption and fluorescence spectra of **3**, **4** and **5** in CH<sub>2</sub>Cl<sub>2</sub> are shown in Fig. 4. The UV/Vis absorption spectrum of **3** shows a slightly broad Soret-like band at λ<sub>max</sub> = 422 nm with two Q-like bands at 580 and 626 nm, respectively. Whereas **4** and **5** showed similar absorption profiles and displayed blue shifted absorption peaks at λ<sub>max</sub> = 375 and 385 nm along with distinct Q-like bands at 572, 621 nm and 582, 631 nm. Upon protonation, both **3** and **4** exhibited a red-shift of the Soret-like

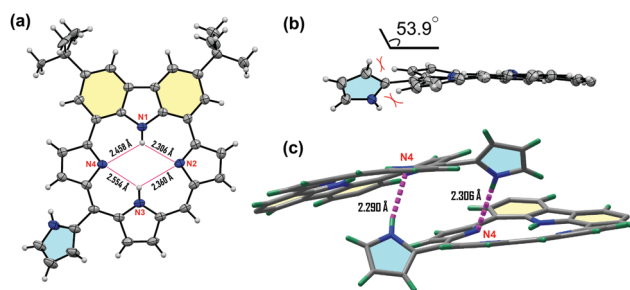


**Fig. 2** Single crystal X-ray structures of macrocycle **3**: (a) a top view showing N–H···N distances, (b) a side view showing the tilting of ring D, and (c) a self-assembled dimer with two intermolecular N–H···N interactions. Solvent molecules and *tert*-butyl groups have been omitted in (b) and (c). Ellipsoids are shown at a 50% probability level.

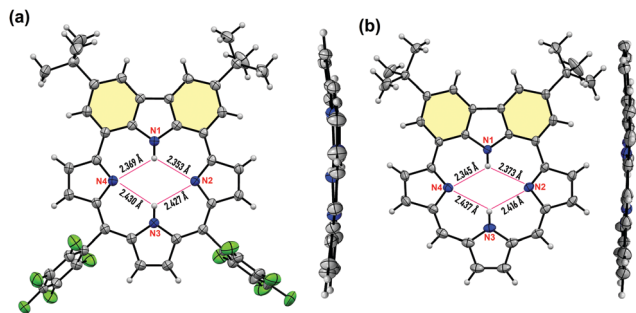


Fig. 3 Single crystal X-ray structures of macrocycles (a) **4** and (b) **5**. Solvent molecules and *meso*-pentafluorophenyl groups have been omitted for clarity in the respective side views. Ellipsoids are shown at a 50% probability level.

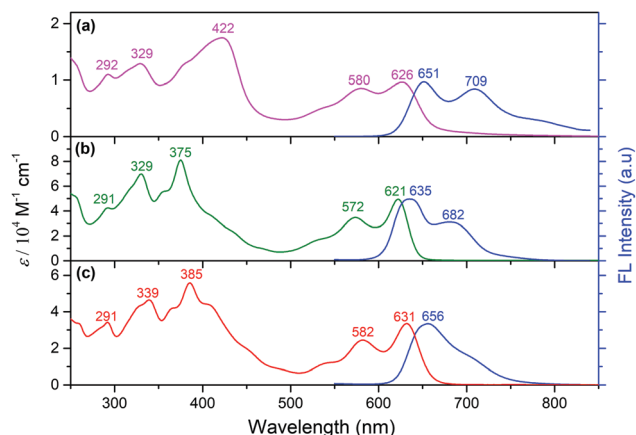


Fig. 4 A comparison of the absorption and fluorescence spectra (blue lines) of macrocycles (a) **3**, (b) **4**, and (c) **5** recorded in  $\text{CH}_2\text{Cl}_2$  at 298 K. All the samples were excited at  $\lambda_{\text{ex}} = 440$  nm.

and Q-like bands with a distinct broadening of the Q-like bands due to the altered HOMO–LUMO levels (Fig. S5.6, ESI<sup>†</sup>). Curiously, **5** did not show a spectral change upon protonation, indicating the weak basicity of the imino-pyrrolic nitrogen due to the strong electron-withdrawing nature of *meso*- $\text{C}_6\text{F}_5$  groups. The fluorescence spectra of **3**, **4** and **5** exhibit a broad emission profile that is notably shifted with respect to the lowest-energy transition (Fig. 4).

We observed two different emission spectra for **3** which are attributed to two different NH tautomers **3T1** and **3T2** generated through a double intramolecular hydrogen transfer (DIHT) (Fig. 1b). The tautomer **3T1** shows two emission maxima at 651 and 709 nm upon excitation in the range of 400–550 nm. We also observed two emission maxima at 773 and 803 nm for the **3T2** tautomer in addition to the **3T1** emission features (Fig. 5a). Notably, the intensities of the **3T2** tautomer increase upon excitation at a longer wavelength, whereas the **3T1** intensities remain unchanged. Further, to confirm the existence of tautomers **3T1** and **3T2** (*trans*-to-*trans*), we recorded the excitation spectra of **5** in  $\text{CH}_2\text{Cl}_2$  at two emission maxima ( $\lambda_{\text{em}} = 651$  and 773 nm). These spectra indicate the presence of two different absorbing species, as evident from two dissimilar excitation

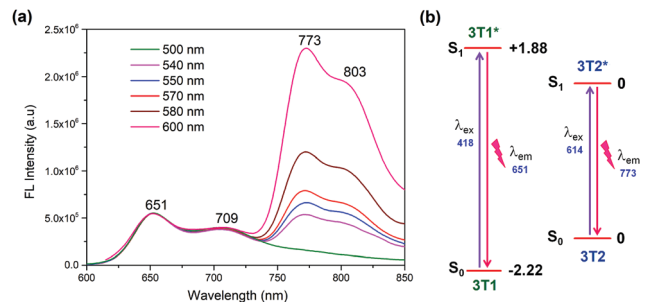


Fig. 5 (a) Emission spectra of **3** recorded at various excitation wavelengths in  $\text{CH}_2\text{Cl}_2$ . Spectra have been normalized at 651 nm. (b) Energy level diagrams of the tautomerism between **3T1** and **3T2** in the ground and excited states, calculated at the B3LYP/6-31g(d) level of theory (units:  $\text{kcal mol}^{-1}$ ). The solvent effect was accounted for using PCM. Excitation and emission wavelengths (units: nm) are also shown.

spectra (Fig. S5.4, ESI<sup>†</sup>). We found a red shifted emission for **3** upon increasing the solvent polarity (Fig. S5.7, ESI<sup>†</sup>). To confirm the NH tautomeric behaviour in **3**, we examined the variable-temperature  $^1\text{H}$  NMR spectra, which showed an indistinguishable proton signal as expected for the existence of a fast interconversion between both tautomeric forms (**3T1** and **3T2**) (Fig. S4.15, ESI<sup>†</sup>). Even at 213 K in  $\text{CDCl}_3$ , we were unable to detect two separate pairs of signals corresponding to the tautomers **3T1** and **3T2**, thus revealing the coexistence of these two NH tautomers. Identical excitation and absorption spectra of macrocycles **4** and **5** confirm the presence of a single species.

We found a bi-exponential feature for the fluorescence decay of **3**, probed at 650 nm, with an average lifetime of 0.26 ns. This bi-exponential feature clearly indicates the presence of two different NH tautomeric forms in the excited state. In contrast, we observed single exponential fluorescence lifetimes of 5.25 and 5.51 ns for **4** and **5**, respectively (Fig. S10.1, ESI<sup>†</sup>). The photophysical properties and kinetic parameters ( $k_r$  and  $k_{nr}$ , respectively) of **3**, **4** and **5** are summarized in (Table S10.1, ESI<sup>†</sup>). Relative fluorescence quantum yields ( $\Phi_F$ ) were determined using a previously reported compound as a reference in toluene.<sup>18,21</sup> The derived  $\Phi_F$  for **4** and **5** were found to be *ca.* 0.309 and 0.261, respectively, which may be attributed to the low rates of intersystem crossing (ISC). Interestingly, the quantum yield varies from *ca.* 0.072 to 0.033 upon changing the excitation wavelength from 440 to 600 nm for **3**. The observed lower  $\Phi_F$  for **3**, compared to those for **4** and **5**, could be due to the strong intermolecular hydrogen bonding between the *meso*-pyrrole NH and the imino-nitrogen of ring C.<sup>22</sup> This is in good agreement with the theoretically calculated oscillator strengths originating from two different tautomers, **3T1** and **3T2** (Fig. S7.4, ESI<sup>†</sup>).

The HOMO–LUMO energy gaps for all these macrocycles were estimated *via* cyclic voltammetry (CV) and differential pulse voltammetry (DPV). Estimated electrochemical HOMO–LUMO (H–L) gaps of 1.82 V for **3**, 1.53 V for **4** and 1.79 V for **5** (Fig. S9.1, ESI<sup>†</sup>) were obtained. All three macrocycles showed irreversible oxidations, but exhibited two consecutive reversible to quasi-reversible reduction waves as judged by both CV and

DPV analysis (Fig. S9.1, ESI<sup>†</sup>). Compared with macrocycles **3** ( $E_{\text{ox1}} = 1.32$  V) and **4** ( $E_{\text{ox1}} = 1.04$  V), the first oxidation of **5** ( $E_{\text{red1}} = 1.51$  V) occurs at a significantly more positive potential. Such an effect is inherent due to the *meso*-pentafluoro substituents of **5** being harder to oxidize and easier to reduce ( $E_{\text{red1}} = -0.28$  V) than those of the *meso*-unsubstituted homologue **4**. No significant change in the reduction potential was observed between **3** ( $E_{\text{red1}} = -0.50$  V) and **4** ( $E_{\text{red1}} = -0.49$  V), signifying a minimal redox change by the introduction of pyrrole at one of the *meso*-position of **4**.

The analysis of frontier molecular orbitals (FMOs) reveals that the highest occupied molecular orbitals (HOMOs) and lowest unoccupied molecular orbitals (LUMOs) of macrocycles **4** and **5** are identical in shape with a similar energy gap (Fig. S8.6, ESI<sup>†</sup>). For all the compounds, the LUMOs are readily isolated from other unoccupied orbitals. The HOMO–LUMO gap for tautomer **3T1** is  $\sim 2.34$  eV and decreases to  $\sim 2.01$  eV for the tautomer **3T2** (Fig. S8.5, ESI<sup>†</sup>). The HOMO and LUMO of **5** are relatively stabilized as compared with those of **3** and **4** due to the electron withdrawing *meso*-C<sub>6</sub>F<sub>5</sub> substituents. The broad absorbances in **3–5** are both composed of transitions that are a mixture of HOMO  $\rightarrow$  LUMO and HOMO–1  $\rightarrow$  LUMO transitions. To further evaluate the aromatic character, we calculated NICS values at the global centre of macrocycles **3**, **4** and **5**, estimated to be  $-2.84$ ,  $-3.29$  and  $-3.58$  ppm, respectively, thereby suggesting the weak aromatic nature of these macrocycles (Fig. S8.1–3, ESI<sup>†</sup>). Further, to evaluate the aromaticity, we conducted an anisotropy of the induced current density (ACID) plot visualizing their distinct clockwise ring current and corroborating its aromatic character (Fig. S10.2, ESI<sup>†</sup>). DIHT calculations employing density functional theory (DFT)<sup>23</sup> provide the relative energy difference between the **3T1** and **3T2** tautomers to be  $2.22$  kcal mol<sup>-1</sup> (Fig. 1 and Table S7.4, ESI<sup>†</sup>). Notably, DIHT can be achieved *via* thermal activation or by a photo-induced process, which are extensively studied in porphycenes.<sup>24</sup> We observed the *meta*-stable *cis* intermediates which facilitates the DIHT as reported previously.<sup>25,26</sup> Other possible tautomeric species involving single or double proton transfer were identified, but were found to be energetically high, making the tautomerism unfavourable, as calculated by DFT (Table S7.4, and Fig. S7.3, ESI<sup>†</sup>).

In conclusion, we synthesized three carbazole embedded porphyrin-like macrocycles **3–5** bearing different *meso*-substituents. Single-crystal X-ray diffraction analyses reveal the planar conformations of macrocycles **4** and **5**, but slight distortion of the macrocyclic plane in **3** with two strong intermolecular N–H $\cdots$ N hydrogen bonding interactions was observed. The combined photophysical and theoretical studies confirm dual emission originating from two tautomers **3T1** and **3T2** having lower symmetry. Further work is ongoing to establish the underlying mechanisms associated with NH tautomerism and the structure of the molecule in the excited state.

This work was supported by IISER Thiruvananthapuram and SERB Core Research Grant No. CRG/2019/006303. A. K. thanks CSIR and A. S. thanks IISER TVM for their fellowships. We thank Alex P. Andrews for solving the X-ray structures of **3**, **4**, and **5**.

## Conflicts of interest

There are no conflicts to declare.

## Notes and references

- 1 T. Kumagai, F. Hanke, S. Gawinkowski, J. Sharp, K. Kotsis, J. Waluk, M. Persson and L. Grill, *Nat. Chem.*, 2014, **6**, 41–46.
- 2 J. N. Ladenthin, T. Frederiksen, M. Persson, J. C. Sharp, S. Gawinkowski, J. Waluk and T. Kumagai, *Nat. Chem.*, 2016, **8**, 935–940.
- 3 M. Drobizhev, N. S. Makarov, A. Rebane, G. de la Torre and T. Torres, *J. Phys. Chem. C*, 2008, **112**, 848–859.
- 4 M. J. Crossley, L. D. Field, M. M. Harding and S. J. Sternhell, *J. Am. Chem. Soc.*, 1987, **109**, 2335–2341.
- 5 J. Braun, M. Schlabach, B. Wehrle, M. Kçcher, E. Vogel and H. H. Limbach, *J. Am. Chem. Soc.*, 1994, **116**, 6593–6604.
- 6 J. Braun, H. H. Limbach, P. G. Williams, H. Morimoto and D. E. Wemmer, *J. Am. Chem. Soc.*, 1996, **118**, 7231–7232.
- 7 R. Gui, H. Jin, X. Bu, Y. Fu, Z. Wang and Q. Liu, *Coord. Chem. Rev.*, 2019, **383**, 82–103.
- 8 Z. Wang, C.-Y. Zhu, J.-T. Mo, X.-Y. Xu, J. Ruan, M. Pan and C.-Y. Su, *Angew. Chem., Int. Ed.*, 2021, **133**, 2556–2563.
- 9 H. L. Lee, H. J. Jang and J. Y. Lee, *J. Mater. Chem. C*, 2020, **8**, 10302–10308.
- 10 X. Ji, R.-T. Wu, L. Long, X.-S. Ke, C. Guo, Y.-J. Ghang, V. M. Lynch, F. Huang and J. L. Sessler, *Adv. Mater.*, 2018, **30**, 1705480.
- 11 M. Luo, X. Li, L. Ding, G. Baryshnikov, S. Shen, M. Zhu, L. Zhou, M. Zhang, J. Lu, H. Ågren, X.-D. Wang and L. Zhu, *Angew. Chem., Int. Ed.*, 2020, **59**, 17018–17025.
- 12 S. M. A. Fateminia, Z. Mao, S. Xu, Z. Yang, Z. Chi and B. Liu, *Angew. Chem., Int. Ed.*, 2017, **56**, 12160–12164.
- 13 A. Vdovin, J. Sepiol, N. Urbanska, M. Pietraszkiewicz, A. Mordzinski and J. Waluk, *J. Am. Chem. Soc.*, 2006, **128**, 2577–2586.
- 14 M. Gil and J. Waluk, *J. Am. Chem. Soc.*, 2007, **129**, 1335–1341.
- 15 M. Kruk, T. H. Ngo, P. Verstappen, A. Starukhin, J. Hofkens, W. Dehaen and W. Maes, *J. Phys. Chem. A*, 2012, **116**, 10695–10703.
- 16 M. Beenken, W. Maes, M. Kruk, T. Martínez and M. Presselt, *J. Phys. Chem. A*, 2015, **119**, 6875–6883.
- 17 A. Takiguchi, S. Kang, N. Fukui, D. Kim and H. Shinokubo, *Angew. Chem., Int. Ed.*, 2021, **60**, 2915–2919, DOI: 10.1002/anie.202013542.
- 18 A. Kalaiselvan, I. S. V. Krishna, A. P. Nambiar, A. Edwin, V. S. Reddy and S. Gokulnath, *Org. Lett.*, 2020, **22**, 4494–4499.
- 19 K. Yamasumi, Y. Notsuka, Y. Yamaoka, S. Mori, M. Ishida and H. Furuta, *Chem. – Eur. J.*, 2020, **26**, 13590–13594.
- 20 P. D. Rao, B. J. Littler, G. R. Geier and J. S. Lindsey, *J. Org. Chem.*, 2000, **65**, 1084–1092.
- 21 C. Maeda, M. Masuda and N. Yoshioka, *Org. Biomol. Chem.*, 2014, **12**, 2656–2662.
- 22 J. Herbich, M. Kijak, A. Zielinska, R. P. Thummel and J. Waluk, *J. Phys. Chem. A*, 2002, **106**, 2158–2163.
- 23 M. J. Frisch *et al.*, *GAUSSIAN 16 (Revision A.03)*, Gaussian, Inc., Wallingford CT, 2016. For the full citations, see ESI<sup>†</sup>.
- 24 T. Kumagai, F. Hanke, S. Gawinkowski, J. Sharp, K. Kotsis, J. Waluk, M. Persson and L. Grill, *Phys. Rev. Lett.*, 2013, **111**, 246101.
- 25 D. K. Maity, R. L. Bell and T. N. Truong, *J. Am. Chem. Soc.*, 2000, **122**, 897–906.
- 26 M. J. Crossley, M. M. Harding and S. Sternhell, *J. Am. Chem. Soc.*, 1986, **108**, 3608–3613.